Titre: Natural olivine crystal-fabrics in the western Pacific convergence region: A new method to identify fabric type
Title:

Auteurs: Katsuyoshi Michibayashi, David Mainprice, Ayano Fujii, Shigeki Uehara, Yuri Shinkai, Yusuke Kondo, Yasuhiko Ohara, Teruaki Ishii, Patricia Fryer, Sherman H. Bloomer, Akira Ishiwatari, James W. Hawkins, & Shaocheng Ji
Authors:

Date: 2016

Type: Article de revue / Article

Référence: Michibayashi, K., Mainprice, D., Fujii, A., Uehara, S., Shinkai, Y., Kondo, Y., Ohara, Y., Ishii, T., Fryer, P., Bloomer, S. H., Ishiwatari, A., Hawkins, J. W., & Ji, S. (2016). Natural olivine crystal-fabrics in the western Pacific convergence region: A new method to identify fabric type. Earth and Planetary Science Letters, 443, 70-80. https://doi.org/10.1016/j.epsl.2016.03.019
Citation:

Titre de la revue: Earth and Planetary Science Letters (vol. 443)
Journal Title:

Maison d'édition: Elsevier
Publisher:

URL officiel: https://doi.org/10.1016/j.epsl.2016.03.019
Official URL:

Earth and Planetary Science Letters 443 (2016) 70–80

Contents lists available at ScienceDirect

Earth and Planetary Science Letters

www.elsevier.com/locate/epsl

Natural olivine crystal-fabrics in the western Pacific convergence region: A new method to identify fabric type

Katsuyoshi Michibayashi [a,b,c,*], David Mainprice [d], Ayano Fujii [a], Shigeki Uehara [a], Yuri Shinkai [a], Yusuke Kondo [a], Yasuhiko Ohara [e,f], Teruaki Ishii [g], Patricia Fryer [h], Sherman H. Bloomer [i], Akira Ishiwatari [j,k], James W. Hawkins [l], Shaocheng Ji [m]

[a] Institute of Geosciences, Shizuoka University, Shizuoka 422-8529, Japan
[b] Graduate School of Science and Technology, Shizuoka University, Shizuoka 422-8529, Japan
[c] Research and Development Center for Ocean Drilling Science, JAMSTEC, Yokosuka, 237-0061, Japan
[d] Géosciences Montpellier, Université Montpellier, 34095 Montpellier cedex 05, France
[e] Hydrographic and Oceanographic Department of Japan, Tokyo 104-0045, Japan
[f] Department of Subsurface Geobiological Analysis and Research, JAMSTEC, Yokosuka, 237-0061, Japan
[g] Center for Integrated Research and Education of Natural Hazards, Shizuoka University, Shizuoka 422-8529, Japan
[h] Department of Geology and Geophysics/SOEST, University of Hawaii at Manoa, Honolulu, HI 96821, USA
[i] College of Earth, Ocean and Atmospheric Sciences, Oregon State University, Corvallis, OR 97331-5506, USA
[j] Kanazawa University, Kanazawa 920-1192, Japan
[k] Center for Northeast Asian Studies, Tohoku University, Sendai 980-8576, Japan
[l] Scripps Institution of Oceanography, UC San Diego, CA 92093, USA
[m] Département des Génies Civil, Géologique et des Mines, École Polytechnique de Montréal, Montréal, Québec, Canada

ARTICLE INFO

Article history:
Received 9 October 2015
Received in revised form 8 March 2016
Accepted 9 March 2016
Available online 24 March 2016
Editor: B. Buffett

Keywords:
mantle
olivine
fabric
Vp-Flinn plot

ABSTRACT

Crystallographic preferred orientations (CPOs) of olivine within natural peridotites are commonly depicted by pole figures for the [100], [010], and [001] axes, and they can be categorized into five well-known fabric types: A, B, C, D, and E. These fabric types can be related to olivine slip systems: A with (010)[100], B with (010)[001], C with (001)[001], D with {0kl}[100], and E with (001)[100]. In addition, an AG type is commonly found in nature, but its origin is controversial, and could involve several contributing factors such as complex slip systems, non-coaxial strain types, or the effects of melt during plastic flow. In this paper we present all of our olivine fabric database published previously as well as new data mostly from ocean floor, mainly for the convergent margin of the western Pacific region, and we introduce a new index named *Fabric-Index Angle* (FIA), which is related to the P-wave property of a single olivine crystal. The FIA can be used as an alternative to classifying the CPOs into the six fabric types, and it allows a set of CPOs to be expressed as a single angle in a range between −90° and 180°. The six olivine fabric types have unique values of FIA: 63° for A type, −28° for B type, 158° for C type, 90° for D type, 106° for E type, and 0° for AG type. We divided our olivine database into five tectonic groups: ophiolites, ridge peridotites, trench peridotites, peridotite xenoliths, and peridotites enclosed in high-pressure metamorphic rocks. Our results show that although our database is not yet large enough (except for trench peridotites) to define the characteristics of the five tectonic groups, the natural olivine fabrics vary in their range of FIA: 0° to 150° for the ophiolites, 40° to 80° for the ridge peridotites, −40° to 100° for the trench peridotites, 0° to 100° for the peridotite xenoliths, and −40° to 10° for the peridotites enclosed in high-pressure metamorphic rocks. The trench peridotites show a statistically unimodal distribution of FIA consisting of the high peak equivalent of the A type, but with some FIAs close to the AG and D types. The variations in the olivine fabrics in the trench peridotites could result from variations in deformation within the supra-subduction uppermost mantle, possibly related to evolution of the mantle since the subduction initiation of the Pacific plate.

1. Introduction

Our understanding of olivine crystallographic preferred orientations (CPOs) has progressed dramatically over the past ~10 yr

* Corresponding author at: Institute of Geosciences, Shizuoka University, Shizuoka 422-8529, Japan.
E-mail address: michibayashi@shizuoka.ac.jp (K. Michibayashi).

http://dx.doi.org/10.1016/j.epsl.2016.03.019

as a result of both natural and experimental studies, as well as major technological developments. An olivine CPO within a peridotite is the expression of the crystal-fabric of olivine grains with respect to its structural framework (x-, y-, and z-axes), and it is the result of plastic flow in the mantle. These olivine CPOs are commonly categorized into five fabric types, A, B, C, D, and E, which have been established based on the results of experimental studies (Fig. 1A; Jung et al., 2006; Karato et al., 2008). The fabric types are generally attributed to the predominant activity of a particular olivine slip system: A with (010)[100], B with (010)[001], C with (001)[001], D with {0kl}[100], and E with (001)[100] (Jung and Karato, 2001; Katayama and Karato, 2004; Jung et al., 2006; Karato et al., 2008). This scheme has proved to be powerful enough to be applied worldwide to natural olivine fabrics (e.g., Mizukami et al., 2004; Skemer et al., 2006; Mainprice, 2007; Karato et al., 2008; Michibayashi and Oohara, 2013).

There exists another olivine fabric type, previously known as the axial-[010] or [010]-fiber pattern (e.g., Ben Ismaïl and Mainprice, 1998; Tommasi et al., 2000; Vauchez and Garrido, 2001; Michibayashi and Mainprice, 2004; Vauchez et al., 2005; Tommasi et al., 2006; Vonlanthen et al., 2006; Le Roux et al., 2007, 2008; Bascou et al., 2008; Tommasi et al., 2008; Tommasi and Vauchez, 2015). Mainprice (2007) named this the AG type, following on from the five fabric types of Karato (Fig. 1A). In simple shear the AG type usually requires at least two slip systems, (010)[100] and (010)[001], whereas in axially symmetric shortening it may result simply from (010)[100] slip (e.g., Holtzman et al., 2003; Michibayashi and Mainprice, 2004). Clearly, we need to consider the AG type in addition to the A to E types.

In nature, it is not always easy to categorize a measured CPO as one of the six fabric types, particularly in the case of weak CPOs or patterns that are highly oblique to the kinematic framework (i.e., foliation and lineation). This difficulty seems also to apply in the interpretation of CPOs developed during deformation experiments, where inverse pole figures have been used to identify olivine fabric types (e.g., Jung et al., 2009). Since three pole figures for the principal crystallographic axes are generally prepared when interpreting a CPO pattern, an alternative approach to the analysis of pole figure symmetry is to determine the three eigenvalues of the normalized orientation matrices in each pole figure (e.g., Satsukawa et al., 2013; Cao et al., 2015). However, this quantitative approach is rather complex, and it is not intuitive when comparing the results with other factors.

In this paper, we present a new method for comparing olivine fabric types. Our method requires the calculation of seismic properties, and in particular the P-wave velocity distribution (Vp), based on olivine CPO data, elastic coefficients, and the density of a single olivine crystal (Mainprice, 1990). We employ a Flinn-type diagram and related diagrams to express the Vp anisotropy for each set of CPO data. We show that our method is successful in providing a quantitative classification of olivine fabric data in conjunction with the six olivine fabric types.

2. Olivine fabric types and the *Vp*-Flinn diagram

Olivine crystals contain intrinsic elastic anisotropies. The development of olivine CPOs within peridotite during plastic deformation gives rise to the seismic anisotropy of the upper mantle (e.g., Nicolas and Christensen, 1987; Nishimura and Forsyth, 1989; Mainprice, 1990; Tommasi et al., 2000; Mainprice, 2007; Michibayashi, 2008; Tommasi and Vauchez, 2015). Both P-wave and S-wave velocity (Vp and Vs, respectively) anisotropies in peridotite are calculated from crystallographic orientation data using a set of programs developed by David Mainprice (e.g., Mainprice, 1990). Since P-wave velocities can be calculated in all directions, the Vp anisotropy (Vp_{anis}) are given by

$$Vp_{anis} = 100 \times \frac{V_{max} - V_{min}}{\frac{V_{max}+V_{min}}{2}},$$

where V_{max} and V_{min} are the maximum and minimum velocities, respectively.

Here, we use three P-wave velocities (V_x, V_y, V_z) in a Flinn diagram with V_y/V_z for the horizontal axis and V_x/V_y for the vertical axis, and its origin as $(1, 1)$ (Flinn, 1962). This method has firstly been introduced by Barberini et al. (2007) and extensively developed by Ji and his colleagues (Ji et al., 2013, 2014, 2015; Shao et al., 2014; Michibayashi, 2015).

To define the field of the six olivine fabric types in the diagram, we should consider the orientations of the three principal axes in the structural framework (x–y–z axes) where the foliation is the x–y plane and the lineation is parallel to the x-axis. Thus, V_x is the velocity parallel to the x-axis, V_y is parallel to the y-axis, and V_z is parallel to the z-axis.

For a single olivine crystal, the maximum Vp is parallel to the a-axis (V_a), whereas the minimum Vp is parallel to the b-axis (V_b). Since Vp parallel to the c-axis (V_c) is perpendicular to both V_a and V_b because of the orthorhombic symmetry of olivine, we consider these three Vp values for a single olivine crystal in a Vp-Flinn diagram.

For an A-type fabric, V_a is parallel to V_x, V_b is parallel to V_z, and V_c is parallel to V_y (Fig. 1B). For a B-type fabric, V_a is parallel to V_y, V_b is parallel to V_z, and V_c is parallel to V_x (Fig. 1B). For C-type, V_a is parallel to V_z, V_b is parallel to V_y, and V_c is parallel to V_x (Fig. 1B). For E-type, V_a is parallel to V_x, V_b is parallel to V_y, and V_c is parallel to V_z (Fig. 1B).

The D-type fabric is characterized by a girdle pattern of both b- and c-axes, and a single point maximum for the a-axis. Therefore, although V_a can be parallel to V_x, both V_b and V_c cannot be parallel to the other two velocities, respectively. Instead, V_y and V_z are equally assumed to be $(V_b + V_c)/2$ (Fig. 1B). Similarly, for the AG-type, V_z is parallel to V_b, and both V_x and V_z are equally assumed to be $(V_a + V_c)/2$ (Fig. 1B). It is noted that although it is possible to assume any other unknown type such as axial-[001] pattern consisting of a girdle pattern of both a- and b-axes, and a single point maximum for the c-axis in a similar way, we simply focus on the known six olivine fabrics from here.

In this study, we derive the P-wave velocities of a single olivine crystal from Abramson et al. (1997), so that V_a is 9.77 km/s, V_b is 7.65 km/s, and V_c is 8.33 km/s. Therefore, it is important to state that P-wave velocities are calculated assuming room pressure and temperature. As a result, the six olivine fabrics for a single olivine crystal are shown in a Flinn diagram (Fig. 1C) where the broken lines are contour lines of a given Vp_{anis} percent.

The angle of inclination between the point of origin $(1, 1)$ and a point in the Flinn diagram is defined by K:

$$K = \frac{\frac{V_x}{V_y} - 1}{\frac{V_y}{V_z} - 1}.$$

However, it is not convenient to use K as commonly used in structural geology, since the Vp-Flinn diagram has three quadrants instead of only one quadrant in a normal Flinn diagram (Flinn, 1962). Thus, we introduce a new index angle, θ, as follows:

$$\theta = \tan^{-1} K.$$

As shown in Fig. 1C, θ has a range between $-90°$ and $180°$ to define the field of each fabric type in the three quadrants. We name this index angle the *Fabric-Index Angle* (FIA). Finally, we obtain the following values of FIA for the six olivine fabric types for a sin-

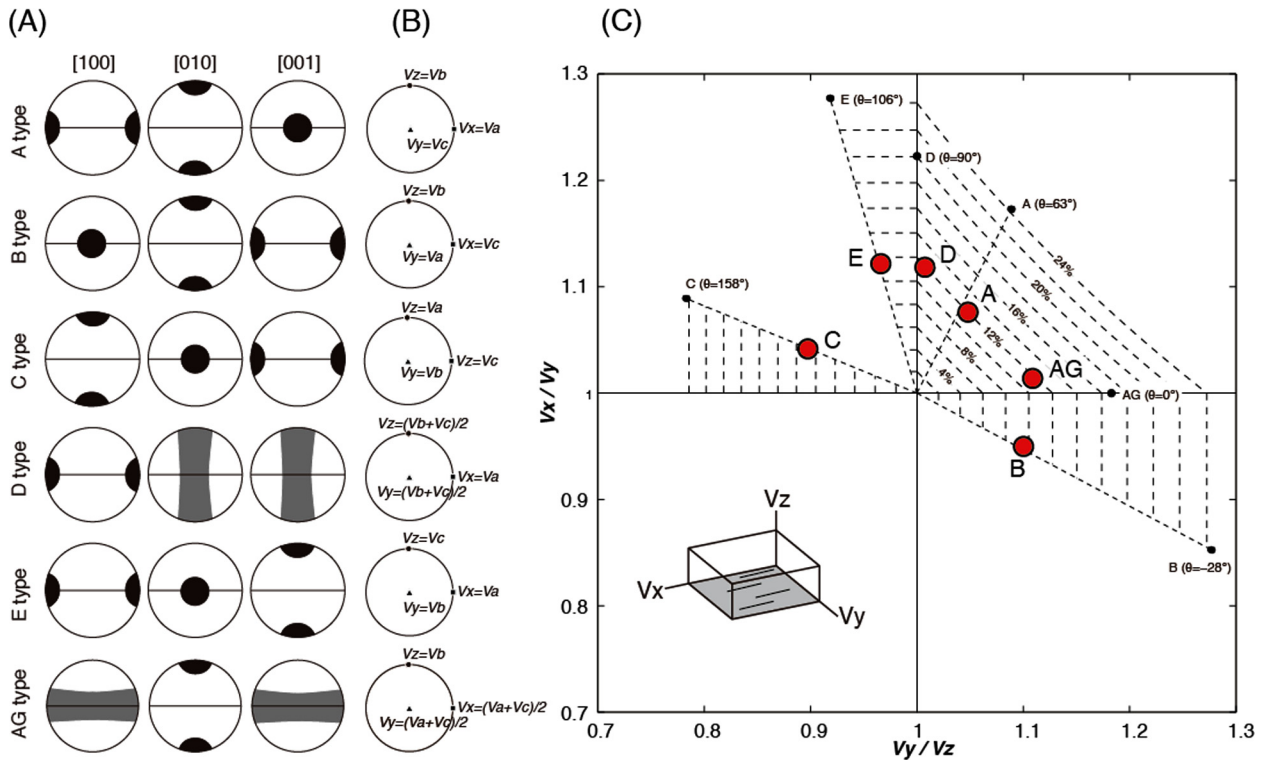

Fig. 1. (A) Six types of olivine crystal-fabrics. (B) Three principal P-wave velocities (*Vp*) with respect to the structural framework shown in the inset of (C) (V_x, V_y, and V_z for *Vp* in the *x*, *y*, and *z* axes, respectively) derived from individual values of three crystallographic axes of a single olivine crystal (V_a for *Vp* in the [100] axis, V_b for *Vp* in the [010] axis, and V_c for *Vp* in the [001] axis). Since the D and AG types are characterized respectively by girdle patterns of the [010] and [001] axes and [100] and [001] axes, their *Vp* values are assumed to be the mean value of the *Vp* in the two crystallographic axes (i.e., $(V_b + V_c)/2$ for the D fabric type, and $(V_a + V_c)/2$ for the AG fabric type). These *Vp* values give us the maximum values for individual fabric types. (C) *Vp*-Flinn plot for the olivine crystal-fabric types. Six olivine crystal-fabric types are plotted as solid black points based on the *Vp* values defined in (B), whereas those shown in Fig. 2 are plotted as large red points. θ is the *Fabric-Index Angle* between the horizontal axis and a line to each point, as the origin is (1, 1). The broken lines are *Vp* anisotropy values defined by the maximum *Vp* and the minimum *Vp*. See the text for further details. (For interpretation of the references to color in this figure legend, the reader is referred to the web version of this article.)

gle olivine crystal: FIA = 63° for A type, −28° for B type, 158° for C type, 90° for D type, 106° for E type, and 0° for AG type (Fig. 1). We are now ready to present our olivine fabric database collected in our laboratory for the last fifteen years using this diagram (Fig. 1C).

3. Olivine fabric database

Our olivine fabric database includes new data from the ocean floor combined with previously published data. About 200 crystal orientations have been measured per sample in highly polished thin sections cut perpendicular to the foliation and parallel to the lineation (i.e. *xz*-section). The foliations (*x*–*y* plane) and lineations (*x*-axis) of the peridotites are defined by the shape-preferred orientation and/or alignment of spinel and/or pyroxene grains. Since the density distributions of crystallographic axes have commonly some angles against the *x*–*y*–*z* axes determined by mineral textures (Fig. 2A), the calculated three P-wave velocities (V_{max}, V_{int}, and V_{min}) also have angles against the *x*–*y*–*z* axes (Fig. 2B). Therefore, we determined V_x, V_y and V_z to be the nearest P-wave velocity among the three values to the *x*–*y*–*z* axes, respectively, as shown in Fig. 2B, whereas we excluded the data that were unclear to determine V_x, V_y and V_z due to too high angles to fit to the *x*–*y*–*z* axes.

The data can be divided into five tectonic groups: ophiolites, ridge peridotites, trench peridotites, peridotite xenoliths, and peridotites in HP metamorphic rocks; most of the data are derived from the western Pacific convergence region (Fig. 3). The ophiolite data are from the Oman ophiolite (Michibayashi and Mainprice, 2004; Michibayashi et al., 2006a, 2006b; Michibayashi and Oohara, 2013) and the Yakuno ophiolite (Michibayashi et al., 2013) (red points in Fig. 3). The few ridge peridotite data we have are from the Godzilla Megamullion (Harigane et al., 2011a) and the Mariana Trough (new data) (magenta points in Fig. 3). The trench peridotite data are from the Bonin (Ogasawara) Trench (Harigane et al., 2013), the South Mariana Trench (Michibayashi et al., 2007, 2009b; new data), the North Mariana Trench (new data), and the Tonga Trench (new data) (blue points in Fig. 3). The peridotite xenolith data are from Ichinomegata (Michibayashi et al., 2006a, 2006b), Avacha (Michibayashi et al., 2009a), Knippa (Satsukawa et al., 2010), Kilbourne Hole (Satsukawa et al., 2011), a petit-spot (Harigane et al., 2011b), and Tasmania (Michibayashi et al., 2012) (green points in Fig. 3). The data for the peridotites in HP metamorphic rocks are from the Imono (Tasaka et al., 2008) and Higashi–Akaishi (Muramoto et al., 2011) massifs (cyan points in Fig. 3).

4. Results

4.1. Olivine fabrics from our database plotted on a Vp-Flinn diagram

Fig. 4 shows the olivine fabrics from our database plotted on a *Vp*-Flinn diagram. Most of the data are distributed in a range of FIA between 0° and 90°, corresponding to olivine fabric types from AG to A to D. The *Vp* anisotropies vary from 4% to 16%, and they tend to be higher in the FIA range between 60° and 90°. The olivine fabric data for the peridotites in HP metamorphic rocks are dominantly distributed in an FIA range between −28° and 0°, corresponding to the fabric types from B to AG. Some of the peridotite xenoliths (M06I and M09A in Fig. 4) are distributed in a range of

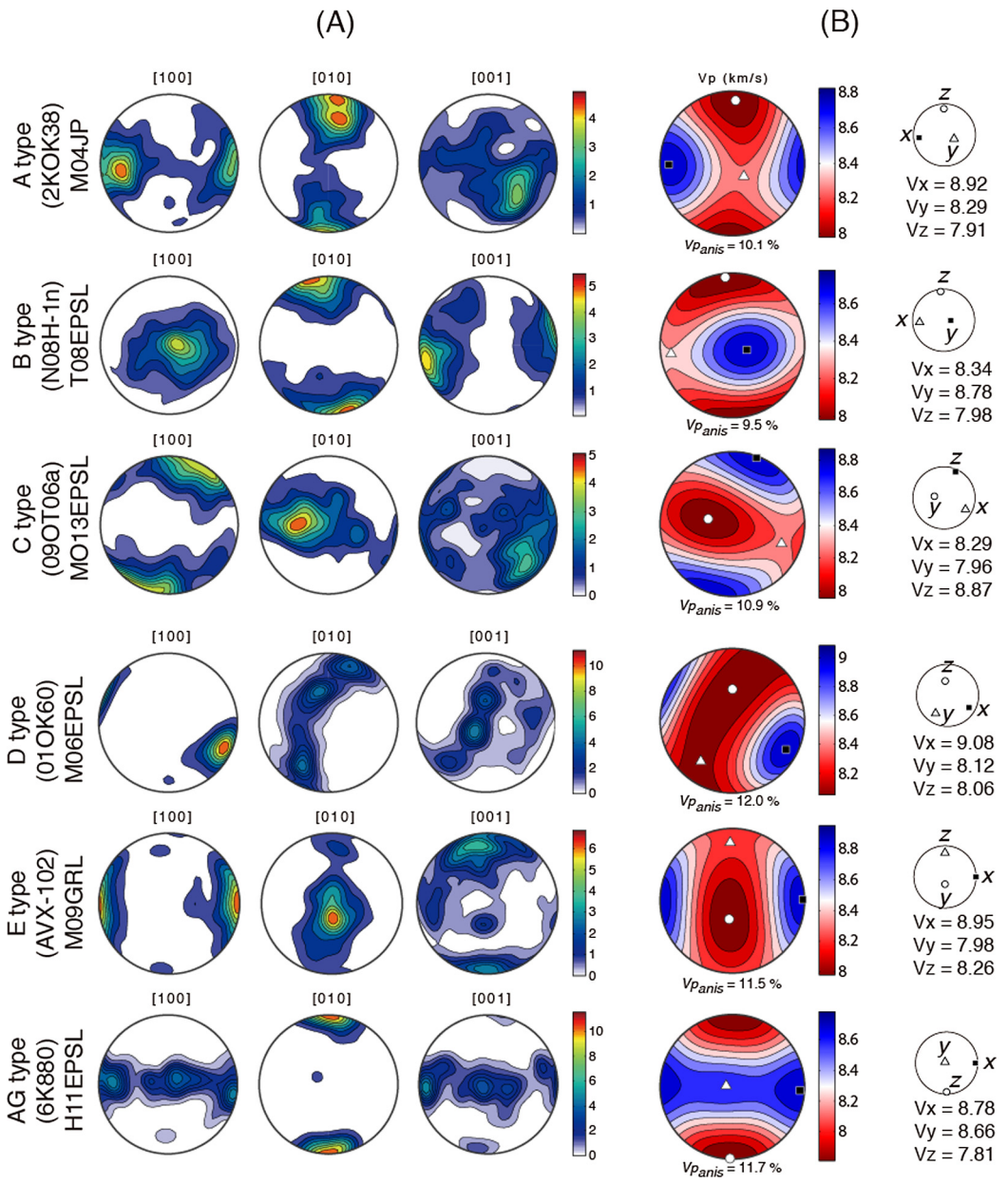

Fig. 2. (A) Typical six types of olivine crystal-fabrics from A type to AG type. Sample no. in each parenthesis with its reference; M04JP: Michibayashi and Mainprice (2004); T08EPSL: Tasaka et al. (2008); MO13EPSL: Michibayashi and Oohara (2013); M06EPSL: Michibayashi et al. (2006b); M09GRL: Michibayashi et al. (2009a); H11EPSL: Harigane et al. (2011a). (B) P-wave velocities calculated from A type to AG type shown in (A). Solid square: the direction of the maximum P-wave velocity; open triangle: the direction of the intermediate P-wave velocity; open circle: the direction of the minimum P-wave velocity.

FIA between 90° and 110° corresponding to the fabric types from D to E. A few olivine data from the Bonin Trench (H13 in Fig. 4) also plot in the same range of FIA between D and E types. Olivine data from the Oman ophiolite (MO13 in Fig. 4), obtained from a traverse of a wet shear zone (Michibayashi and Oohara, 2013), plot in the E- and C-type areas.

4.2. Relationship to fabric intensities

Exponential relationships are observed between fabric intensities (J-index and M-index) and *Vp* anisotropy (Fig. 5), indicating that the *Vp* anisotropy can be interpreted as a kind of fabric intensity parameter. The data in Fig. 5 suggest that the peridotites in HP metamorphic rocks have different trends from the other four groups in our olivine fabric database, although the number of the samples is as low as 18 (the inset in Fig. 3).

5. Interpretation

5.1. Transformation of the Vp-Flinn diagram to FIA–Vp anisotropy space

The *Vp*-Flinn diagram in Fig. 4 is convenient for presenting all the olivine fabrics from our database together. However, the data points become more widely spaced towards higher *Vp* anisotropies, and the density distribution of the olivine fabrics in the database therefore becomes weaker, even though the number of points for low and high *Vp* anisotropies are equal on the *Vp*-Flinn diagram. To overcome this limitation, we transformed the data plots from the *Vp*-diagram to those in FIA-*Vp* anisotropy space (Fig. 6A), where the *Vp*-anisotropy can also represent the degree of fabric intensity, as shown in Fig. 5.

The *Vp* anisotropies are clearly higher in a range of FIA between 60° and 110° (Fig. 6A), corresponding to olivine fabric types from

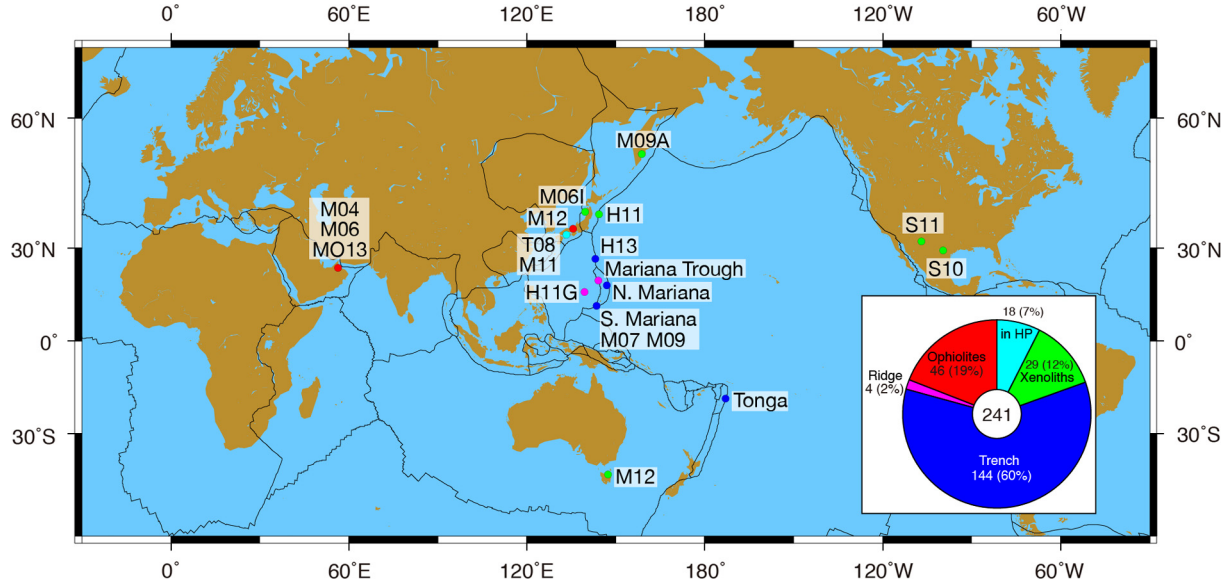

Fig. 3. World map showing the locations of peridotites used in this study (Mariana Trough, N. Mariana, S. Mariana, and Tonga) and in previous studies (M04, M06, M06I, M07, T08, M09, M09A, S10, M11, H11, H11G, S11, M12, and MO13; see below for definitions of these abbreviations) published by the Michibayashi Laboratory at Shizuoka University. The color of each site represents the tectonic setting: red for ophiolite, magenta for ridge peridotite in an ocean, blue for trench peridotite in an ocean, green for peridotite xenolith, and cyan for peridotite entrained in high-pressure (HP) metamorphic rocks. The numbers in the inset are the total number of samples (in the central circle) and the number of samples and percentage of total samples for each tectonic setting. M04, Michibayashi and Mainprice (2004); M06, Michibayashi et al. (2006a); M06I, Michibayashi et al. (2006b); M07, Michibayashi et al. (2007); T08, Tasaka et al. (2008); M09, Michibayashi et al. (2009a); M09A, Michibayashi et al. (2009b); S10, Satsukawa et al. (2010); M11, Muramoto et al. (2011); H11, Harigane et al. (2011a); H11G, Harigane et al. (2011b); S11, Satsukawa et al. (2011); M12, Michibayashi et al. (2012); MO13, Michibayashi and Oohara (2013). (For interpretation of the references to color in this figure, the reader is referred to the web version of this article.)

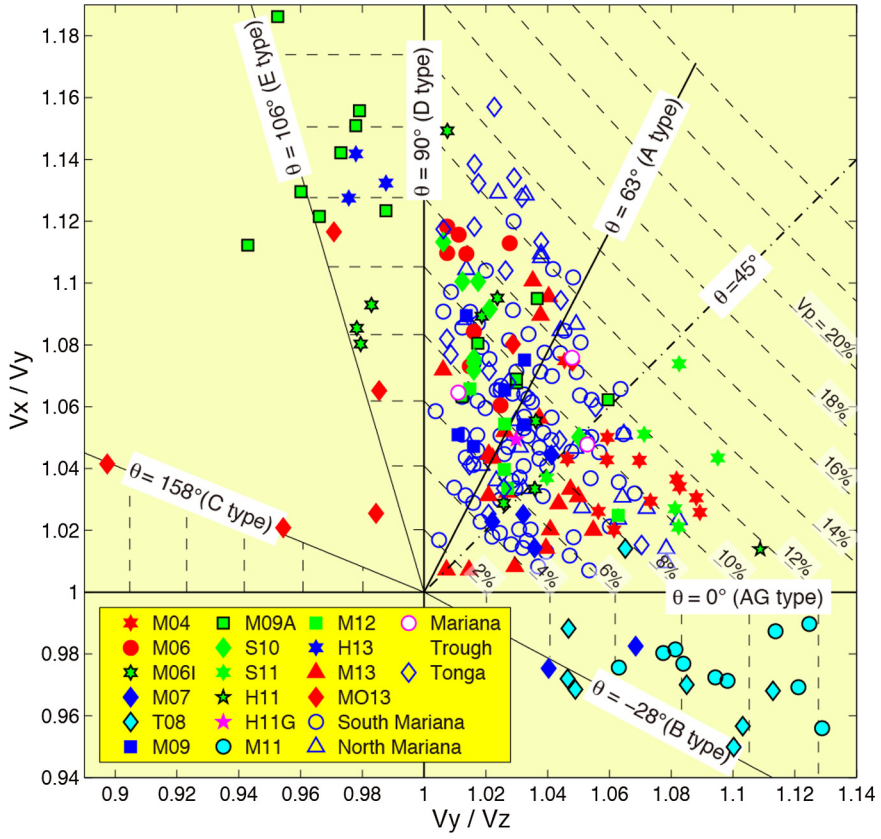

Fig. 4. *Vp*-Flinn diagram for peridotite samples studied by the Michibayashi Laboratory of Shizuoka University. Symbol colors and abbreviations are as in Fig. 3.

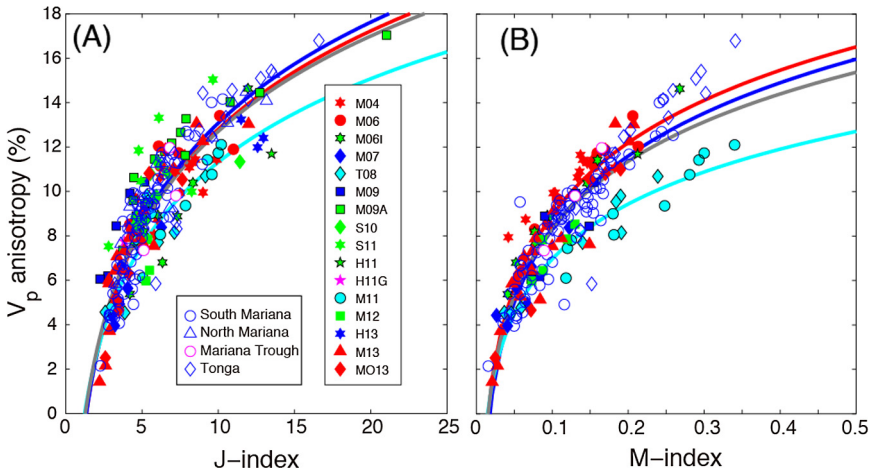

Fig. 5. Fabric intensities vs. *Vp* anisotropy. Symbol colors and abbreviations are as in Fig. 3. (A) J-index. (B) M-index. Black, red, blue and cyan lines in both (A) and (B) show exponential curves for all plotted data, the ophiolite, the trench peridotites, and the peridotites in HP rocks, respectively. Note that exponential curves for the peridotites in HP rocks are distinctively different from the others in both (A) and (B).

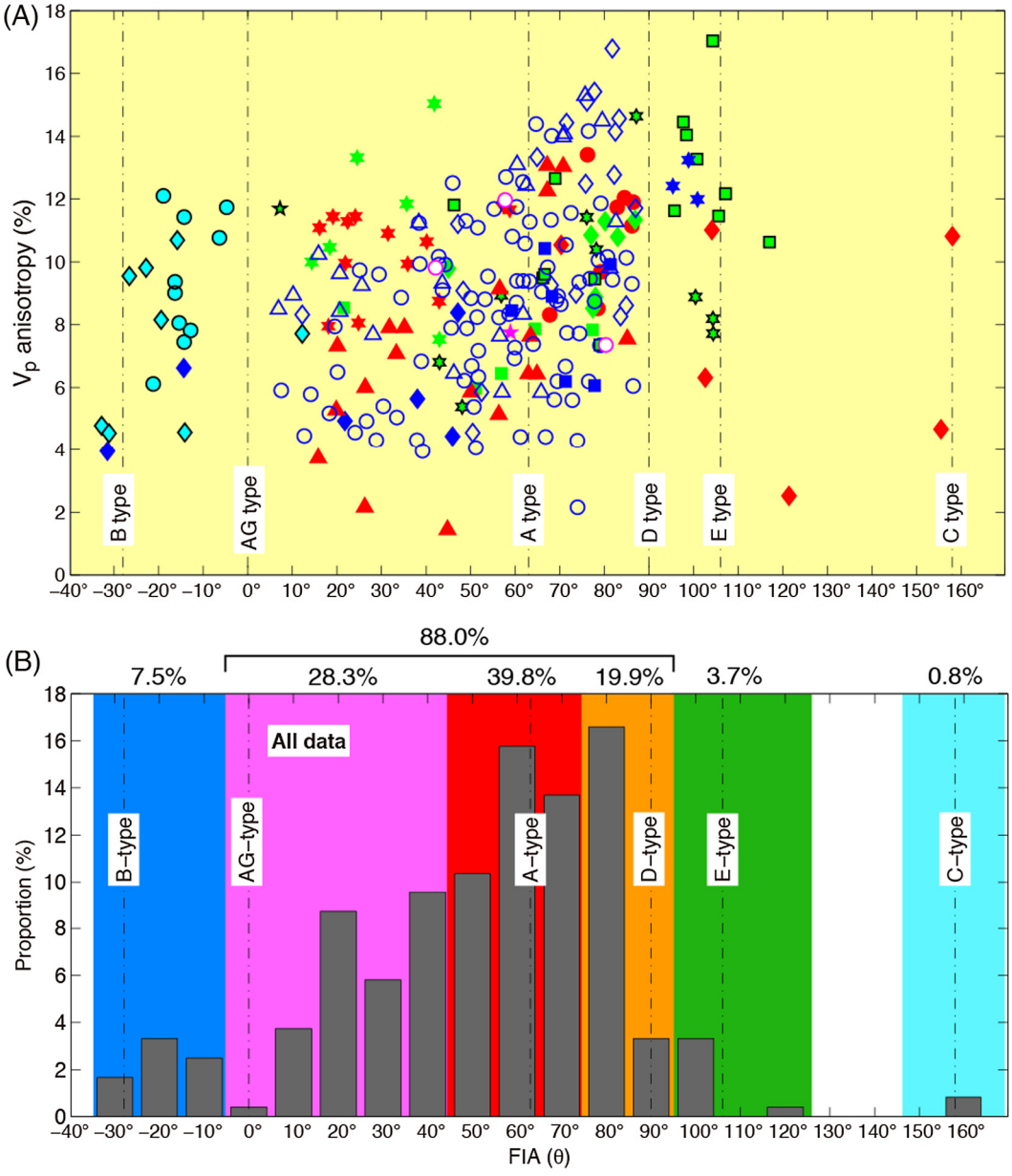

Fig. 6. Fabric-index angle (FIA) vs. *Vp* anisotropy. Symbol colors and abbreviations are as in Fig. 3. (B) Proportions of the six fabric types with respect to FIA.

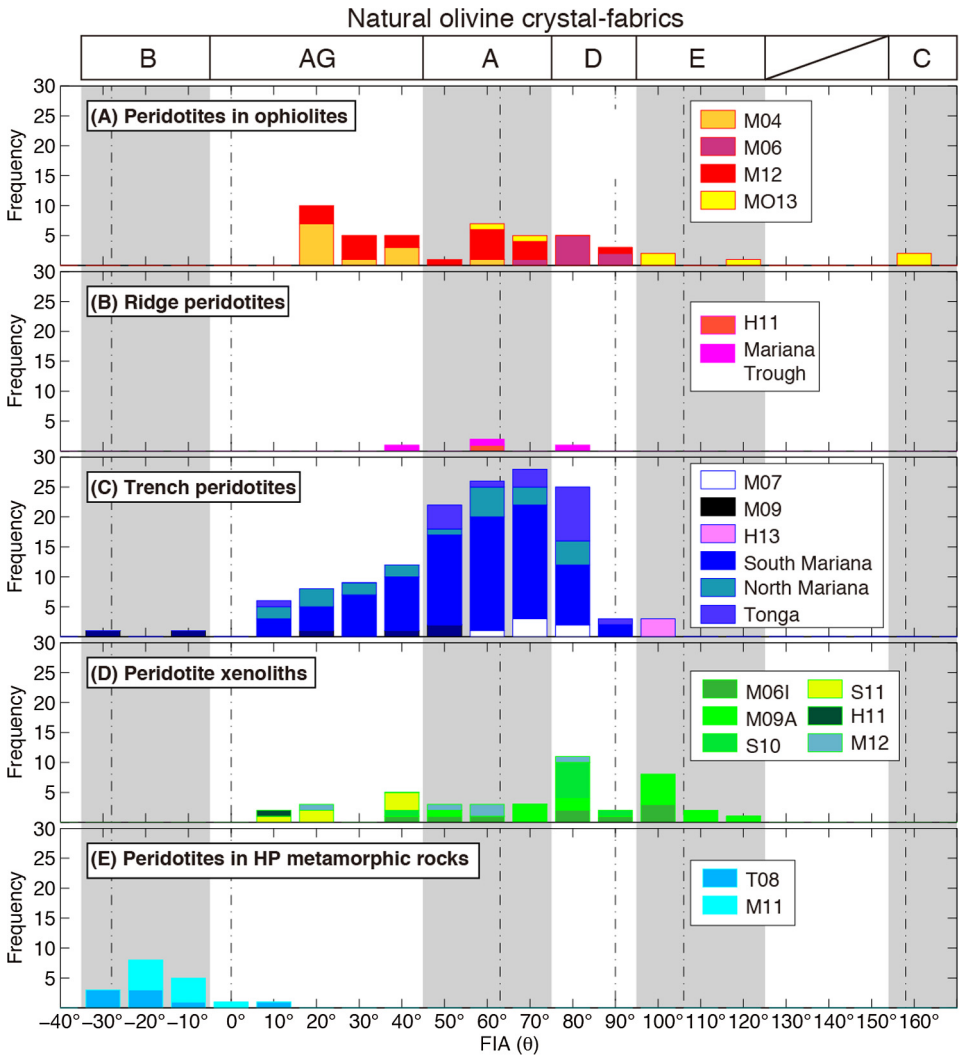

Fig. 7. Frequency histograms of the Fabric-index angle (FIA) for each tectonic setting. Abbreviations are as in Fig. 3.

A to D to E. Furthermore, the peridotites in HP metamorphic rocks are distributed dominantly in the FIA range of −30° to 0°, corresponding to olivine fabric types from B to AG.

5.2. Empirical distribution of olivine fabric types

It is possible to compare just the frequency of FIA distributions, as shown in Fig. 6B, although we lose the information on both *Vp* anisotropies and the degree of fabric intensity. It shows clearly that the natural olivine fabrics are not perfectly fit to the six theoretical types from A to AG in Fig. 6B. For practical usage, it is better to separate the range of FIA into six fabric domains as shown in Fig. 6B. Although the range of FIA for each fabric type is tentative, olivine fabrics in the A-type domain are the most common occurrence of about 40%. The second common occurrence of olivine fabrics is in the AG-type domain with nearly 30%. The third common occurrence of olivine fabrics is in the D-type domain with almost 20%. The olivine fabrics within these three domains occupy nearly 90% of our database (Fig. 6B). It is interesting to note that the distribution of the olivine fabric types in Fig. 6B is almost compatible with those for the other database published by Mainprice (2007) and Tommasi and Vauchez (2015).

Fig. 7 shows the distributions of FIA and the six fabric types for the five tectonic groups, revealing that the olivine fabrics have different characteristics among those tectonic groups. The ophiolites show a distribution with two peaks of FIA: 60° and 20° corresponding to A type and AG type, respectively (Fig. 7A). Despite only a few data points, the FIAs for the ridge peridotites are in the range of 40° to 80°, suggesting they might be dominated by A type (Fig. 7B). The trench peridotites show a large number of data clustered around 60° (i.e. A type) (Fig. 7C). These FIA values are dominantly between 50° and 80°, corresponding to A to D types with a small number of FIAs lower than 30° and higher than 90° (Fig. 7C). The peridotite xenoliths show a broad distribution of FIAs between 10° and 120° with peaks at 40°, 80°, and 100° corresponding to A type, D type and E type, respectively (Fig. 7D). The peridotites in HP metamorphic rocks show a unimodal distribution of FIAs between −30° and 10°, which are dominated by B type (Fig. 7E).

6. Discussion

6.1. Natural olivine fabrics along the western Pacific convergence region

Our olivine fabric data were derived mainly from the western Pacific convergence region, as shown in Fig. 3. We can classify the convergence region into two tectonic cross-sections: Northeast Japan and Mariana (Fig. 8). The Northeast Japan cross-section has no peridotite in the forearc; petit-spot volcanoes occur on the outer-rise region of the subducting Pacific plate (Fig. 8A; e.g.,

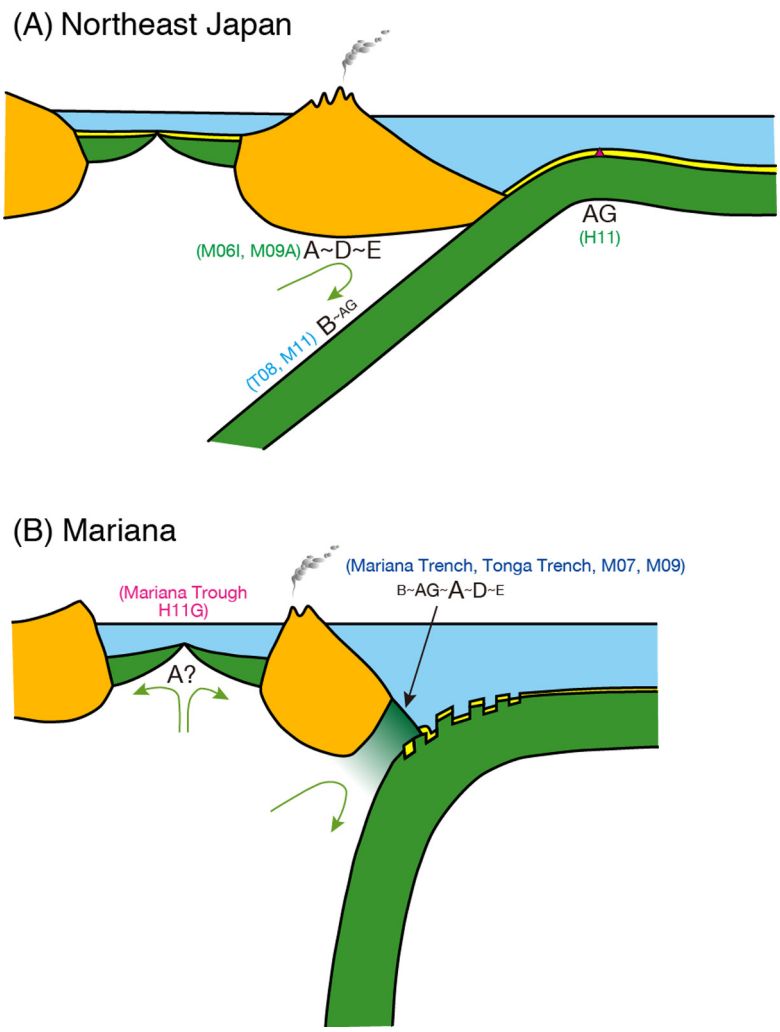

Fig. 8. Schematic cross-sections of the West Pacific convergence margin (modified after Ida and Uyeda, 1981) showing the occurrences of natural olivine crystal-fabric types. (A) Northeast Japan cross-section. (B) Mariana cross-section. Orange is continental crust; dark green is lithospheric mantle; yellow is seafloor sediment. The red triangle in (A) is a petit-spot volcano. Font sizes used for the crystal-fabric types reflect the abundance of the fabric types in natural peridotites, as shown in Fig. 7. The abbreviations (e.g., M07) and colors of the text in parentheses are as in Fig. 3. Olivine fabric types show dominant types such as A∼D based on the occurrence in Fig. 7. The green arrows are assumed flow in mantle. (For interpretation of the references to color in this figure legend, the reader is referred to the web version of this article.)

Hirano et al., 2006). The Mariana cross-section has peridotites in the trench; the subducting Pacific plate is remarkably fractured, resulting in horst and graben structures (Fig. 7B; Uyeda and Kanamori, 1979; Ida and Uyeda, 1981). Our olivine fabric data can now be fitted onto these two cross-sections.

For the northeast Japan cross-section, two peridotite xenoliths (M06I and M09A) derived from Ichinomegata back-arc volcano (Michibayashi et al., 2006a, 2006b; Satsukawa and Michibayashi, 2014) and Avacha volcano (Michibayashi et al., 2009a; Soustelle et al., 2010), respectively, could represent an area beneath the island arc and have fabric types from A to D to E types in Fig. 7D. One peridotite xenolith (H11) had been entrained in magma erupted from petit-spot volcano, so it could have been derived from the lithosphere–asthenosphere boundary (Hirano et al., 2001, 2004, 2006), representing AG type (Harigane et al., 2011b). The peridotites entrained in the HP metamorphic rocks (T08 and M11) were possibly derived from the deep mantle wedge above the subducting slab, where B type may be dominant (Mizukami et al., 2004; Tasaka et al., 2008; Muramoto et al., 2011).

For the Mariana type, our data for the trench peridotites are most reliable among the five tectonic groups in the case of large numbers of data (Fig. 7C). 100 trench peridotites show a broad distribution from B to E types, with a dominant peak of A to D types (Figs. 7C and 8B), although the occurrence of B type was predicted for both the Mariana and Tonga trenches by Jung and Karato (2001). Harigane et al. (2013) argued that E type is the earliest fabric to form during the initiation of subduction, but its occurrence is rare. Nonetheless, the variations in the olivine fabrics in the trench peridotites could result from variations in deformation within the supra-subduction uppermost mantle, possibly related to evolution of the mantle since the subduction initiation of the Pacific plate.

The ridge peridotites we studied are actually back-arc peridotites, such as from the Mariana trough and Parece Vera rift (e.g., Harigane et al., 2011a), and they are mostly A type (Figs. 7B and 8B). However, it should be noted that there are only four data points in our database.

Our results reveal the occurrence of AG type in various tectonic settings: the lithosphere–asthenosphere boundary, the trench region, and the region above the subducting slab (Figs. 7 and 8). Among the olivine fabric types, the AG type may result from various factors such as type of strain, the effect of melt during deformation, or the simultaneous activity of various dislocations (e.g., Harigane et al., 2011b; Tommasi and Vauchez, 2015; Wang et al., 2016).

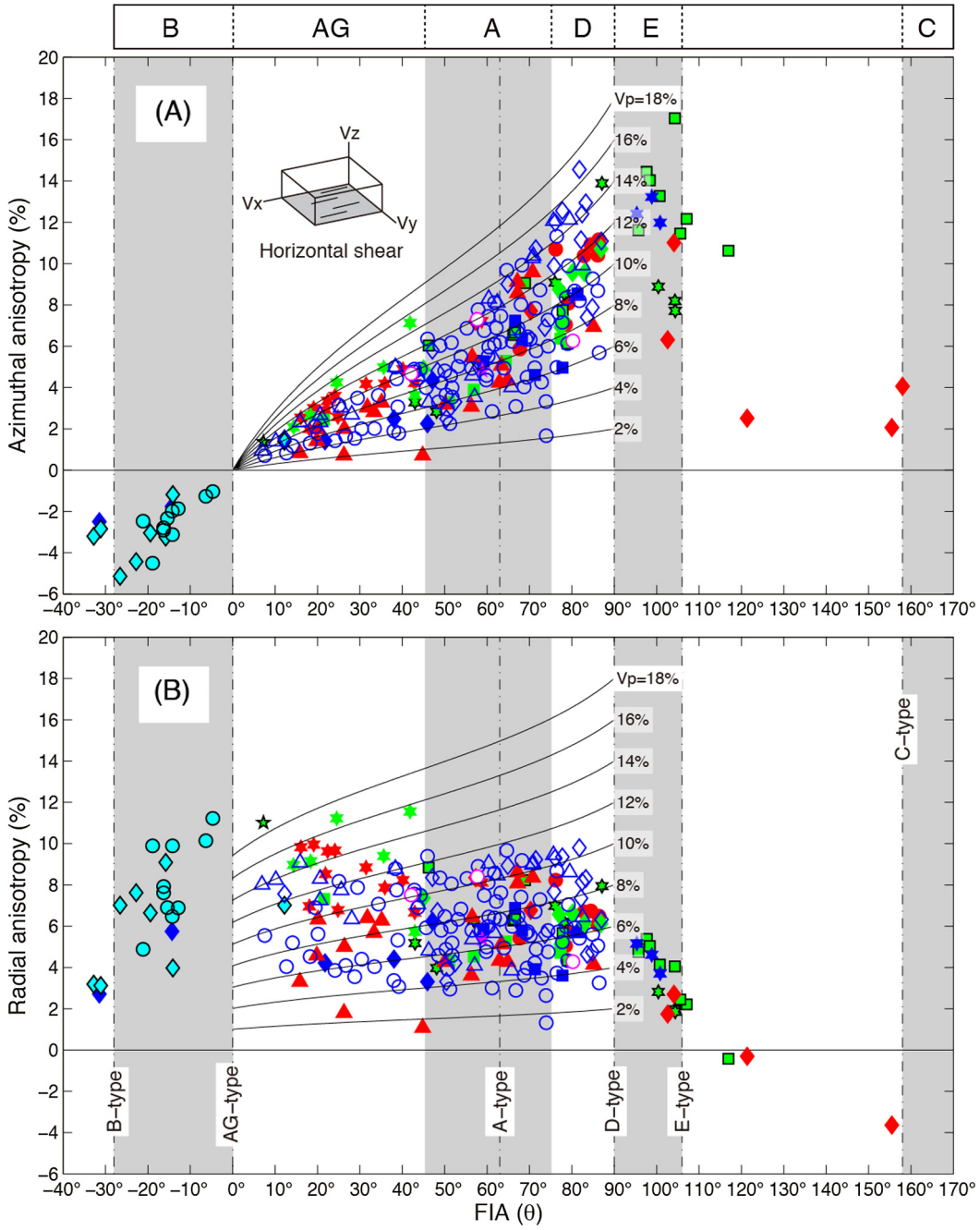

Fig. 9. (A) The Fabric-index angle (FIA) vs. Azimuthal anisotropy (%) between V_x and V_y, assuming a horizontal shear (the inset). (B) The Fabric-index angle (FIA) vs. Radial anisotropy (%) between $(V_x + V_y)/2$ and V_z, assuming a horizontal shear. The thin lines between 0° and 90° are *Vp* anisotropy values defined by the maximum *Vp* and the minimum *Vp*.

6.2. *Presumed olivine fabrics in the Pacific plate*

Seismic observations have extensively been conducted in the northwestern Pacific Ocean, where is composed of the oldest oceanic crust on Earth (Shimamura et al., 1983; Shinohara et al., 2008; Oikawa et al., 2010; Kodaira et al., 2014). Shimamura et al. (1983) reported 4–7% azimuthal anisotropy at 40–140 km depth, whereas Shinohara et al. (2008) detected 5% and 13% azimuthal anisotropy at 8–10 km depth and 40–50 km depth, respectively. Oikawa et al. (2010) presented 7–10% azimuthal anisotropy within 5 km immediately below the Moho. More recently, Kodaira et al. (2014) identified strong azimuthal anisotropy of 8.5–9.8% in the uppermost mantle immediately below the Moho. Variation in azimuthal anisotropy observed in the Pacific Plate can be attributed to the dependence on the spreading rate (e.g., Oikawa et al., 2010; Song and Kim, 2012).

In the seismic results, the direction of higher P-wave velocity is perpendicular to the paleomagnetic lineation, so that it is generally believed that the azimuthal anisotropy is caused by olivine CPOs in mantle when the oceanic plate was created at the mid-ocean spreading center (e.g., Hess, 1964; Raitt et al., 1969). In Fig. 9, we show a relationship between FIA and calculated azimuthal anisotropy as well as calculated radial anisotropy, assuming a horizontal shear. Since the direction of higher P-wave velocity is subparallel to the direction of the Plate motion, it may be likely to assume that olivine fabric types are between FIA = 0° (AG type) and FIA = 90° (D type; Nishimura and Forsyth, 1989) in Fig. 9. It shows that azimuthal anisotropy increases from 0° to 90°

(Fig. 9A), indicating its direct relationship to olivine fabric types. Consequently, variation of azimuthal anisotropy in the Pacific Plate could result from variation of olivine fabric types; the region of higher azimuthal anisotropy in mantle (e.g., Oikawa et al., 2010; Kodaira et al., 2014) could be dominated by A to D types, whereas the region of the lower azimuthal anisotropy in mantle (e.g., Shinohara et al., 2008) could be characterized by AG-type (Fig. 9A). It is interesting to note that there is few difference in radial anisotropy between FIA = 0° and FIA = 90° in contrast to azimuthal anisotropy (Fig. 9B).

Acknowledgements

The pole figures were made using the MATLAB M-file based on programs of MTEX version 4 (http://mtex-toolbox.github.io/). We thank the captain and crew of the *R/V Yokosuka*, *Kairei* and *Hakuho-maru*, the scientific parties and our colleagues for their continuous support and cooperation during this study and Phil Skemer and Takehiko Hiraga for their thoughtful comments. KM sincerely thanks to students and graduates in his laboratory contributed to the database presented in this paper. This study was supported by research grants awarded to KM by the Japan Society for the Promotion of Science (Kiban-B 16340151, Kiban-B 19340148 and Kiban-A 22244062).

References

Abramson, E.H., Brown, J.M., Slutsky, L.J., Zang, J.J., 1997. The elastic constants of San Carlos olivine to 17 GPa. J. Geophys. Res. 102, 12253–12263.

Barberini, V., Burlini, L., Zappone, A., 2007. Elastic properties, fabric and seismic anisotropy of amphibolites and their contribution to the lower crust reflectivity. Tectonophysics 445, 227–244.

Bascou, J., Delpech, G., Vauchez, A., Moine, B.N., Cottin, J.Y., Barruol, G., 2008. An integrated study of microstructural, geochemical, and seismic properties of the lithospheric mantle above the Lerguelen plume (Indian Ocean). Geochem. Geophys. Geosyst. 9, Q04036.

Ben Ismaïl, W., Mainprice, D., 1998. A statistical view of the strength of seismic anisotropy in the upper mantle based on petrofabric studies of Ophiolite and xenolith samples. Tectonophysics 296, 145–157.

Cao, Y., Jung, H., Song, S., Park, M., Jung, S., Lee, J., 2015. Plastic deformation and seismic properties in fore-arc mantles: a petrofabric analysis of the Yushigou harzburgites, North Qilian Suture Zone, NW China. J. Petrol. 56, 1897–1944.

Flinn, D., 1962. On folding during three-dimensional progressive deformation. Q. J. Geol. Soc. 118, 385–428.

Harigane, Y., Michibayashi, K., Ohara, Y., 2011a. Relicts of deformed lithospheric mantle within serpentinites and weathered peridotites from the Godzilla Megamullion, Parece Vela Back-Arc Basin, Philippine Sea. Isl. Arc 20, 174–187.

Harigane, Y., Mizukami, T., Morishita, T., Michibayashi, K., Abe, N., Hirano, N., 2011b. Direct evidence for upper mantle structure within the NW Pacific Plate: microstructural analyses of a petit-spot peridotite xenolith. Earth Planet. Sci. Lett. 302, 194–202.

Harigane, Y., Michibayashi, K., Morishita, T., Tani, K., Dick, H., Ishizuka, O., 2013. The earliest mantle fabrics formed during subduction zone infancy. Earth Planet. Sci. Lett. 377–378, 106–113.

Hess, H.H., 1964. Seismic anisotropy of the uppermost mantle under oceans. Nature 203, 629–631.

Hirano, N., Kawamura, K., Hattori, M., Saito, K., Ogawa, Y., 2001. A new type of intraplate volcanism; young alkali-basalts discovered from the subducting Pacific Plate, northern Japan Trench. Geophys. Res. Lett. 28, 2719–2722.

Hirano, N., Yamamoto, J., Kagi, H., Ishii, T., 2004. Young, olivine xenocryst-bearing alkali basalt from the oceanward slope of the Japan Trench. Contrib. Mineral. Petrol. 148, 47–54.

Hirano, N., Takahashi, E., Yamamoto, J., Abe, N., Ingle, S.P., Kaneoka, K., Kimura, J., Hirata, T., Ishii, T., Ogawa, Y., Machida, S., Suyehiro, K., 2006. Volcanism in response to plate fexture. Science 313, 1426–1428.

Holtzman, B., Kohlstedt, D.L., Zimmerman, M.E., Heidelbach, F., Hiraga, T., Hustoft, J., 2003. Melt segregation and strain partitioning: implications for seismic anisotropy and mantle flow. Science 301, 1227–1230.

Ida, Y., Uyeda, S., 1981. The mechanism of plate subduction. Iwanami-Kagaku 51, 481–489 (in Japanese).

Ji, S., Shao, T., Michibayashi, K., Long, C.X., Wang, Q., Kondo, Y., Zhao, H.C. Wang, Salisbury, M.H., 2013. A new calibration of seismic velocities, anisotropy, fabrics, and elastic moduli of amphibole-rich rocks. J. Geophys. Res., Solid Earth 118, 4699–4728.

Ji, S., Shao, T., Salisbury, M.H., Sun, S.S., Michibayashi, K., Zhao, W.H., Long, C.X., Liang, F.H., Satsukawa, T., 2014. Plagioclase crystal preferred orientation and induced seismic anisotropy. J. Geophys. Res., Solid Earth 119, 8064–8088.

Ji, S., Shao, T., Michibayashi, K., Oya, S., Satsukawa, T., Wang, Q., Zhao, W., Salisbury, M.H., 2015. Magnitude and symmetry of seismic anisotropy in mica- and amphibole-bearing metamorphic rocks and implications for tectonic interpretation of seismic data from the southeast Tibetan Plateau. J. Geophys. Res., Solid Earth 120. http://dx.doi.org/10.1002/2015JB012209.

Jung, H., Karato, S.-I., 2001. Water-induced fabric transitions in olivine. Science 293, 1460–1463.

Jung, H., Katayama, I., Jiang, Z., Hiraga, T., Karato, S., 2006. Effect of water and stress on the lattice-preferred orientation of olivine. Tectonophysics 421, 1–22.

Jung, H., Mo, W., Green, H.W., 2009. Upper mantle seismic anisotropy resulting from pressure-induced slip transition in olivine. Nat. Geosci. 2, 73–77.

Karato, S., Jung, H., Katayama, I., Skemer, P.A., 2008. Geodynamic significance of seismic anisotropy of the upper mantle: new insights from laboratory studies. Annu. Rev. Earth Planet. Sci. 36, 59–95.

Katayama, I., Karato, S., 2004. A new type of olivine fabric at modest water content and low stress. Geology 32, 1045–1048.

Kodaira, S., Fujie, G., Yamashita, M., Sato, T., Takahashi, T., Takahashi, N., 2014. Seismological evidence of mantle flow driving plate motions at a plaeo-spreading centre. Nat. Geosci. 7, 371–375.

Le Roux, V., Bodinier, J.L., Tommasi, A., Alard, O., Dautria, J.M., Vauchez, A., Riches, A., 2007. The Lherz spinel-lherzolite: refertilized rather than pristine mantle. Earth Planet. Sci. Lett. 259, 599–612.

Le Roux, V., Tommasi, A., Vauchez, A., 2008. Feedback between melt percolation and deformation in an exhumed lithosphere–asthenosphere boundary. Earth Planet. Sci. Lett. 274, 401–413.

Mainprice, D., 1990. A Fortran program to calculate seismic anisotropy from the lattice preferred orientation of minerals. Comput. Geosci. 16, 385–393.

Mainprice, D., 2007. Seismic anisotropy of the deep Earth from a mineral and rock physics perspective. In: Price, G.D. (Ed.), Mineral Physics. In: Schubert, G. (Ed.), Treatise on Geophysics, vol. 2.

Michibayashi, K., 2008. Structure sensitivity and elastic anisotropy within peridotites. J. Geogr. (Chigaku Zasshi) 117, 93–109 (in Japanese with English abstract).

Michibayashi, K., 2015. Olivine crystallographic fabrics and their P-wave velocity structures within peridotites in the uppermost mantle. J. Geogr. (Chigaku Zasshi) 124, 397–409 (in Japanese with English abstract).

Michibayashi, K., Mainprice, D., 2004. The role of pre-existing mechanical anisotropy on shear zone development within oceanic mantle lithosphere: an example from the Oman ophiolite. J. Petrol. 45, 405–414.

Michibayashi, K., Oohara, T., 2013. Olivine fabric evolution in a hydrated ductile shear zone at the Moho Transition Zone, Oman Ophiolite. Earth Planet. Sci. Lett. 377–378, 299–310.

Michibayashi, K., Abe, N., Okamoto, A., Satsukawa, T., Michikura, K., 2006a. Seismic anisotropy in the uppermost mantle, back-arc region of the northeast Japan arc: petrophysical analyses of Ichinomegata peridotite xenoliths. Geophys. Res. Lett. 33, L10312.

Michibayashi, K., Ina, T., Kanagawa, K., 2006b. The effect of dynamic recrystallization on olivine fabric and seismic anisotropy: insights from a ductile shear zone in the Oman ophiolite. Earth Planet. Sci. Lett. 244, 695–708.

Michibayashi, K., Tasaka, M., Ohara, Y., Ishii, T., Okamoto, A., Fryer, P., 2007. Variable microstructure of peridotite samples from the southern Mariana Trench: evidence of a complex tectonic evolution. Tectonophysics 444, 111–118.

Michibayashi, K., Oohara, Y., Satsukawa, T., Ishimaru, S., Arai, S., Okrugin, V.M., 2009a. Rock seismic anisotropy of the low velocity zone beneath the volcanic front in the mantle wedge. Geophys. Res. Lett. 36, L12305.

Michibayashi, K., Ohara, Y., Stern, R.J., Fryer, P., Kimura, J.-I., Tasaka, M., Harigane, Y., Ishii, T., 2009b. Peridotites from a ductile shear zone within backarc lithospheric mantle, southern Mariana Trench: results of a Shinkai6500 dive. Geochem. Geophys. Geosyst. 10, Q05X06. http://dx.doi.org/10.1029/2008GC002197.

Michibayashi, K., Kusafuka, Y., Satsukawa, T., Nasir, S., 2012. Seismic properties of peridotite xenoliths as a clue to imaging the lithospheric mantle beneath NE Tasmania, Australia. Tectonophysics 522–523, 218–223.

Michibayashi, K., Suzuki, M., Komori, N., 2013. Progressive deformation partitioning during the deformation and recrystallization of olivine in the lithospheric mantle. Tectonophysics 587, 79–88.

Mizukami, T., Wallis, S.R., Yamamoto, J., 2004. Natural examples of olivine lattice preferred orientation patterns with a flow-normal a-axis maximum. Nature 427, 432–436.

Muramoto, M., Michibayashi, K., Ando, J., Kagi, H., 2011. Rheological contrast between garnet and clinopyroxene in the mantle wedge: an example from Higashi-akaishi peridotite mass, SW Japan. Phys. Earth Planet. Inter. 84, 14–33.

Nicolas, A., Christensen, N.I., 1987. Formation of anisotropy in upper mantle peridotites: a review. In: Fuchs, K., Froidevaux, C. (Eds.), Composition, Structure and Dynamics of the Lithosphere–Asthenosphere System. In: Geodynamics Series, vol. 16. AGU, pp. 111–123.

Nishimura, C.E., Forsyth, D.W., 1989. The anisotropic structure of the upper mantle in the Pacific. Geophys. J. 96, 203–229.

Oikawa, M., Kaneda, K., Nishizawa, A., 2010. Seismic structures of the 154–160 Ma oceanic crust and uppermost mantle in the Northwest Pacific Basin. Earth Planets Space 62, e13–e16.

Raitt, R.W., Shorr, G.G., Francis, T.J.G., Morris, G.B., 1969. Anisotropy of the Pacific upper mantle. J. Geophys. Res. 74, 3095–3109.

Satsukawa, T., Michibayashi, K., 2014. Flow in the uppermost mantle during back-arc spreading revealed by Ichinomegata peridotite xenoliths, NE Japan. Lithos 189, 89–104.

Satsukawa, T., Michibayashi, K., Raye, U., Anthony, E.Y., Pulliam, J., Stern, R.J., 2010. Uppermost mantle anisotropy beneath the southern Laurentian margin: evidence from Knippa peridotite xenoliths, Texas. Geophys. Res. Lett. 37, L20312, 5 pp.

Satsukawa, T., Michibayashi, K., Anthony, E.Y., Stern, R.J., Gao, S.S., Liu, K.H., 2011. Seismic anisotropy of the uppermost mantle beneath the Rio Grande rift: evidence from Kilbourne Hole peridotite xenoliths, New Mexico. Earth Planet. Sci. Lett. 311, 172–181.

Satsukawa, T., Ildefonse, B., Mainprice, M., Morales, L.F.G., Michibayashi, K., Barou, F., 2013. A database of plagioclase crystal preferred orientations (CPO) and microstructures – implications for CPO origin, strength, symmetry and seismic anisotropy in gabbroic rocks. Solid Earth 4, 511–542.

Shao, T., Ji, S., Kondo, Y., Michibayashi, K., Wang, Q., Xu, Z., Marcotte, D., Salisbury, M.H., 2014. Antigorite-induced seismic anisotropy and implications for deformation in subduction zones and the Tibetan Plateau. J. Geophys. Res., Solid Earth 119. http://dx.doi.org/10.1002/2013JB010661.

Shimamura, H., Asada, T., Suyehiro, K., Yamada, T., Inatani, H., 1983. Longshot experiments to study velocity anisotropy in the oceanic lithosphere of the northwestern Pacific. Phys. Earth Planet. Inter. 31, 348–362.

Shinohara, M., Fukano, T., Kanazawa, T., Araki, E., Suyehiro, K., Mochizuki, M., Nakahigashi, K., Yamada, T., Mochizuki, K., 2008. Upper mantle and crustal seismic structure beneath the Northwestern Pacific Basin using a seafloor borehole broadband seismometer and ocean bottom seismometers. Phys. Earth Planet. Inter. 170, 95–106.

Skemer, P.A., Katayama, I., Karato, S., 2006. Deformation fabrics of a peridotite from Cima di Gagnone, central Alps, Switzerland: evidence of deformation under water-rich condition at low temperatures. Contrib. Mineral. Petrol. 152, 43–51.

Song, A., Kim, Y., 2012. Anisotropic uppermost mantle in young subducted slab underplating Central Mexico. Nat. Geosci. 5, 55–59.

Soustelle, V., Tommasi, A., Demouchy, S., Ionov, D.A., 2010. Deformation and fluid-rock interaction in the supra-subduction mantle: microstructures and water contents in peridotite xenoliths from the Avacha volcano, Kamchatka. J. Petrol. 51, 363–394.

Tasaka, M., Michibayashi, K., Mainprice, D., 2008. B-type olivine fabrics developed in the fore-arc side of the mantle wedge along a subducting slab. Earth Planet. Sci. Lett. 272, 747–757.

Tommasi, A., Vauchez, A., 2015. Heterogeneity and anisotropy in the lithospheric mantle. Tectonophysics 661, 11–37.

Tommasi, A., Mainprice, D., Canova, G., Chastel, Y., 2000. Viscoplastic self-consistent and equilibrium-based modeling of olivine lattice preferred orientations: implications for the upper mantle seismic anisotropy. J. Geophys. Res., Solid Earth 105 (B4), 7893–7908.

Tommasi, A., Vauchez, A., Godard, M., Belley, F., 2006. Deformation and melt transport in a highly depleted peridotite massif from the Canadian Cordillera: implications to seismic anisotropy above subduction zones. Earth Planet. Sci. Lett. 252, 245–259.

Tommasi, A., Vauchez, A., Ionov, D.A., 2008. Deformation, static recrystallization, and reactive melt transport in shallow subcontinental mantle xenoliths (Tok Cenozoic volcanic field, SE Siberia). Earth Planet. Sci. Lett. 272, 65–77.

Uyeda, S., Kanamori, H., 1979. Back-arc opening and the mode of subduction. J. Geophys. Res. 84, 1049–1061.

Vauchez, A., Garrido, C., 2001. Seismic properties of an asthenospherized lithospheric mantle above a mantle plume: constraints from lattice preferred orientations in peridotite from the Ronda massif. Earth Planet. Sci. Lett. 192, 235–249.

Vauchez, A., Dineur, F., Rudnick, R., 2005. Microstructure, texture and seismic anisotropy of the lithospheric mantle above a mantle plume: insights from the Labait volcano xenoliths (Tanzania). Earth Planet. Sci. Lett. 232, 295–314.

Vonlanthen, P., Kunze, K., Burlini, L., Grobety, B., 2006. Seismic properties of the upper mantle beneath Lanzarote (Tanzania). Earth Planet. Sci. Lett. 232, 295–314.

Wang, L., Blaha, S., Pintér, Z., Farla, R., Kawazoe, T., Miyajima, N., Michibayashi, K., Katsura, T., 2016. Temperature dependence of [100](010) and [001](010) dislocation mobility in natural olivine. Earth Planet. Sci. Lett. 441, 81–90.